**SANDIA REPORT**
SAND20XX-XXXX
Printed Click to enter a date

Sandia National Laboratories

# Challenges and Potential of Waveform Modeling for Crustal Scale Predictions

Robert W. Porritt
Andrea C. Conley

Prepared by
Sandia National Laboratories
Albuquerque, New Mexico
87185 and Livermore,
California 94550

Issued by Sandia National Laboratories, operated for the United States Department of Energy by National Technology & Engineering Solutions of Sandia, LLC.

Available to DOE and DOE contractors from
U.S. Department of Energy
Office of Scientific and Technical Information
P.O. Box 62
Oak Ridge, TN 37831

Telephone: (865) 576-8401
Facsimile: (865) 576-5728
E-Mail: reports@osti.gov
Online ordering: http://www.osti.gov/scitech

Available to the public from
U.S. Department of Commerce
National Technical Information Service
5301 Shawnee Rd
Alexandria, VA 22312

Telephone: (800) 553-6847
Facsimile: (703) 605-6900
E-Mail: orders@ntis.gov
Online order: https://classic.ntis.gov/help/order-methods/

# ABSTRACT

Waveform modeling is crucial to improving our understanding of observed seismograms. Forward simulation of wavefields provides quantitative methods of testing interactions between complicated source functions and the propagation medium. Here, we discuss three experiments designed to improve understanding of high frequency seismic wave propagation. First, we compare observed and predicted travel times of crustal phases for a set of real observed earthquakes with calculations and synthetic seismograms. Second, we estimate the frequency content of a series of nearly co-located earthquakes of varying magnitude for which we have a relatively well-known 1D velocity model. Third, we apply stochastic perturbations on top of a 3D tomographic model and qualitatively assess how those variations map to differences in the seismograms. While different in scope and aim, these three vignettes illustrate the current state of crustal scale waveform modeling and the potential for future studies to better constrain the structure of the crust.

This page left blank.

## CONTENTS

## LIST OF FIGURES

# ACRONYMS AND DEFINITIONS

| Abbreviation | Definition |
|---|---|
| P | Compressional |
| S | Shear |
| 1D | One-dimensional |
| 2D | Two-dimensional |
| 2.5D | A 2D model that gives a 3D perspective |
| 3D | Three-dimensional |
| $P_g$ | A compressional seismic wave which bottoms in the middle-crust |
| $P_n$ | A compressional seismic wave which is refracted along the crust-mantle interface |
| UUSS | University of Utah Seismograph Stations |
| Moho | Seismic crust-mantle boundary or Mohorovičić Discontinuity |
| km | Kilometers |
| km/s | Kilometers per second |
| RSTT | Regional Seismic Travel Time 2.5D model |
| CWT | Continuous Wavelet Transform |
| M | Earthquake Magnitude (type agnostic) |
| Hz | Hertz |
| $S_n$ | A compressional seismic wave which is refracted along the crust-mantle interface |
| Vp | Compressional wavespeed of a medium |

# 1. INTRODUCTION

The propagation of seismic waves through the crust can vary significantly due to the heterogeneous structure of the shallow subsurface. This variation can lead to major challenges when trying to understand small seismic events recorded at local to near regional scales, where only high frequency body waves can be readily observed. Analysts are trained to pick first-break compression (P) wave arrivals or distinctive shear (S) wave arrivals and these arrival times can be inverted to determine the location of a seismic event. However, this inversion process is dependent on the algorithm used to infer the ray path through the crust and the wavespeed structure of the crust. As the ray path is dependent on the structure of the propagation medium and the source location is dependent on the ray path, the inversion can quickly become a non-linear problem. The non-linearity of the problem can lead to the use of simplifying assumptions, such as using one-dimensional (1D) wavespeed structure for the ray path and travel time predictions, or different approaches to the problem, such as back-projection. However, well-calibrated three-dimensional (3D) wavespeed models and wave propagation models should provide more accurate earthquake locations.

One way to address the improvement of analysis methods is through the application of synthetic wavefield methods. These tools propagate a known seismic source through a known structure and therefore facilitate analysis of synthetic waveforms based on known propagation parameters. However, these methods are most effective at low frequencies, where small-scale structural heterogeneities can be aggregated into a smooth, long-wavelength structure. Therefore, the current frontier is assessing the efficacy of these methods at high frequencies relevant to the local to near-regional scale (e.g., Olsen et al., 2018; Takemura et al., 2020). These assessments typically focus on the characteristics of the waveforms, but another useful approach is to assess parameters and measurements which can be derived from waveforms, such as P wave arrival times. Furthermore, estimating P wave arrival times from synthetic waveforms can provide a qualitative understanding of how observed arrival times map to subsurface structure.

The mapping of travel time observations to wavespeed structure is typically done through a tomographic inversion. At the scale of the crust, tomographic inversion is often done with local earthquake tomography in regions with significant natural seismicity (i.e., active fault zones or volcanoes) and can achieve resolution on the scale of ~5 km x 5 km x 5 km (e.g., Thurber, 1992; Lanza et al., 2020 and references therein). Due to the non-linearity discussed above, inversion is often done in conjunction with earthquake relocation (e.g., Zhang and Thurber, 2003). This joint source and structure inversion can be iterated with updated ray paths to produce a better fit to the observed data, but it remains to be quantified how well these models can predict future observations at the crustal scale due to the significant structural heterogeneity.

In this report, we seek to assess the variability of crust and uppermost mantle P wave phases (i.e., $P_g$ and $P_n$) observed at the local to near-regional scale. In the first section, we extend an analysis performed by Rowe et al. (2009), which assessed travel time variability for mantle phases, to crustal scale phases. Using a dataset of events with manual picks from analysts at the University of Utah Seismograph Stations (UUSS) and tools to compute expected arrival times as well as tools to compute synthetic seismograms, we quantify the accuracy (mean residual) and precision (standard deviation of residuals) of travel time predictions. In the second section, we quantify the frequency content of body waves and surface waves for a mainshock-aftershock sequence of earthquakes in Oklahoma. In our previous report, we were able to replicate seismograms from the mainshock at periods of a few tens of seconds, but higher frequency waveform fits for smaller magnitude events has proven challenging and we expect this is due to their frequency content. In the third section, we explore the effects of stochastic scattering on synthetic waveforms. Recent work by Olsen et al. (2018) has shown promise at replicating the amplitude of seismograms for an underground nuclear test by incorporating high frequency crustal attenuation and stochastic scattering, but a more detailed exploration of the parameter space is required. Taken together, this report summarizes some of the primary strengths of waveform modeling and helps motivate future directions that can be taken to improve our modeling results.

# 2. EMPIRICAL COMPARISON OF CRUSTAL TRAVEL TIMES

In this analysis, we focus on a set of ~30 events in Utah recorded by the UUSS with phase arrivals determined by their analysts. These events are located with one of three regional 1D wavespeed models depending on the initial location (https://quake.utah.edu/earthquake-information-products/earthquake-catalogs/catalog-details/computation-of-uuss-earthquake-locations-1981-present; accessed 09/02/2021). These models all contain a low wavespeed zone in the upper ~1 km while most of the wavespeed within the crust is ~6 km/s. This model is similar to the AK135 model (Kennett et al., 1995) which has a wavespeed of 5.8 km/s in the upper 20 km and a wavespeed of 6.5 km/s below that to the crust-mantle boundary (Moho) at 35 km. No action was taken to separate events by source (quarry blast vs. earthquake or focal mechanism) and uncertainties were not considered. Therefore, this is not a set of ground-truth events. Nonetheless, we treat them as the standard to compare against while noting their methodological dependence on a model similar to AK135.

In the first case, we consider the difference between the observed travel times and those calculated with TauP (Buland and Chapman, 1983; Crotwell et al., 1999) using the AK135 model and the Regional Seismic Travel Time model (RSTT; Myers et al., 2010; Begnaud et al., 2020) which uses a pseudo-raybending method through a 2.5D tomographic crustal P and $P_n$ model. Figure 2-1 shows observed and calculated arrival times as a function of distance. The observations and two predictions appear to agree well at this visual scale.

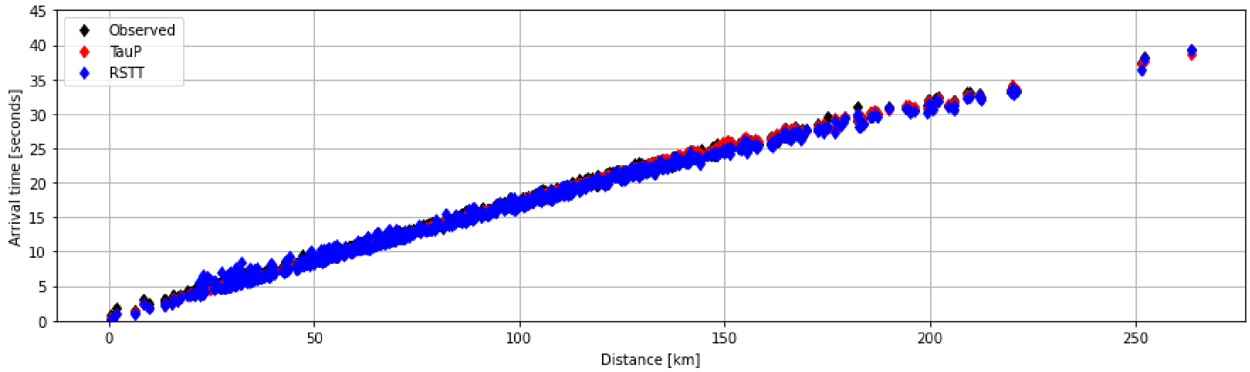

**Figure 2-1: Observed and calculated travel times for a subset of stations and events from the UUSS catalog. Generally, travel times estimated by the two prediction methods, TauP and RSTT, overlap with the observed forming a linear trend of arrival time increasing with distance.**

Considering the residual between the analyst determined arrival times and the predicted times removes the linear trend of arrival time increasing with distance. Figure 2-2 shows the distributions of the residuals and summary statistics. In both cases, the histograms show a negative skew with longer tails towards negative (prediction earlier than observed) residuals. While the standard deviations of these two distributions are about the same (0.40 for TauP vs. 0.48 for RSTT), the mean residual is about three times higher for RSTT (0.10 vs. 0.32). The simplest explanation for this observation is that the events are located by analysts at UUSS with a model similar to AK135 whereas the wavespeed model component of RSTT was developed independently through a tomographic inversion. Therefore, the travel time prediction used in the location process by UUSS is optimized to a wavespeed model similar to AK135. It is further worth noting that the mean residual for the RSTT prediction of 0.32 seconds is similar to the mean mantle P phase residuals of 0.38 and 0.34 seconds observed in Rowe et al. (2009) for predictions based on AK135 with and without CRUST2.0 (Laske et al., 2001) for ground-truth events.

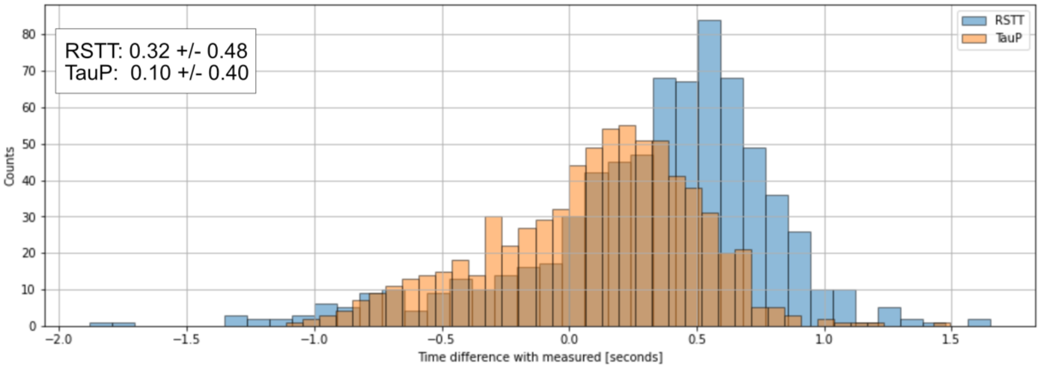

**Figure 2-2: Histograms of residuals between the travel-time prediction and UUSS observations with mean and 1 standard deviation indicated in the upper left.**

We can increase our dataset beyond the analyst picks by using synthetic seismograms. We apply a 2D finite differences algorithm (Vidale, et al., 1985; Li et al., 2014) to replicate the 30 Utah events based on three different wavespeed structures: AK135, CRUST 1.0 (Laske et al., 2013), and a local earthquake tomography model for Utah (Preston and Hoots, Personal Communication). We then hand-picked arrival times on those synthetics to generate an expanded synthetic dataset which contains information about both the expected travel times through a variety of models as well as uncertainties that can be expected from hand-picking. The distributions of residuals shown in Figure 2-3 indicate that the hand-picked arrivals on the AK135 synthetics are biased by -0.05 seconds with a standard deviation of 0.05 seconds relative to the TauP calculation. While other analysts with different picking tools may be able to achieve more accurate or precise measurements, this represents a reasonable baseline for what manual measurements can achieve when subject to complications such as emergent signals, background noise, and cycle skipping. We also note in Figure 2-3 that the mean residual for RSTT has decreased by 0.08 seconds relative to the residuals with UUSS analyst picks. As this value is close to the mean residual for AK135 as seen in Figure 2-2, we suspect this reflects the effect of the different wavespeed models (i.e., 1D AK135 vs. the tomographic 2.5D model of RSTT).

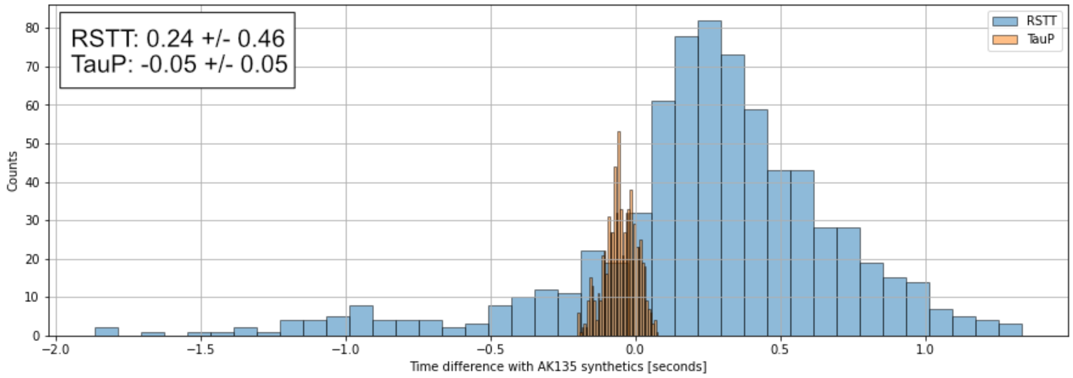

**Figure 2-3: Histograms of residuals between the travel time hand measured on a set of synthetics calculated with a 2D finite difference algorithm and the predicted arrival times from RSTT and TauP with AK135. Mean and 1 standard deviation indicated in the upper left.**

This analysis can be extended to a larger variety of models and prediction methods. These are displayed in Figure 2-4. In all cases when the wavespeed model and prediction model are different (i.e., all cases except AK135 Synthetics vs. TauP prediction [Fig. 2-4d]), we notice an uncertainty of ~0.4 to ~0.5 s. Furthermore, aside from the cases of CRUST1.0 versus TauP (Fig. 2-4e) and versus the UUSS observations (Fig. 2-4h), all mean values are within 1 standard deviation of 0. Considering the accuracy of the models as represented by the mean of the residuals, we can observe 3 approximate regimes. Mean values less than +/-0.2 seconds (tomography vs. RSTT [Fig. 2-4c], tomography vs TauP [Fig. 2-4f], and AK135 vs. UUSS picks [Fig. 2-4g]) are the most accurate. As mentioned above, UUSS uses wavespeed models similar to AK135 for locating the tested events and therefore there is some interdependence between the AK135 synthetics and UUSS picks. The similarity between the tomography-based synthetics and RSTT and TauP is more surprising, but because the mean values are roughly 0.3 seconds apart (+0.16 seconds vs. -0.14 seconds) this suggests the tomographic model is somewhere between these two larger scale models. There is another grouping of distributions between with means of +/-0.2 seconds to +/-0.3 seconds (AK135 synthetics vs. RSTT [Fig. 2-4a], CRUST1.0 synthetics vs. RSTT [Fig. 2-4b], and tomography synthetics vs. UUSS observed [Fig. 2-4i]). These are cases where the wavespeed model is inconsistent with the model used for location. Therefore, we cannot expect the ray paths and travel times to match, but they provide an expectation of misfit for mismatched models. Finally, there are two inaccurate instances where the mean is outside a standard deviation of 0 and these are cases where the synthetics are calculated based on CRUST1.0 and we compare against TauP and the UUSS picks [Fig. 2-4e, h]. The CRUST1.0 synthetics arrive significantly early, which suggests the P waves take a longer ray path through the high wavespeed lower crust in CRUST1.0 than would be predicted with TauP and the AK135 model. However, it is worth noting that these synthetics had more coda and emergent arrivals than other models making their manual picks less certain.

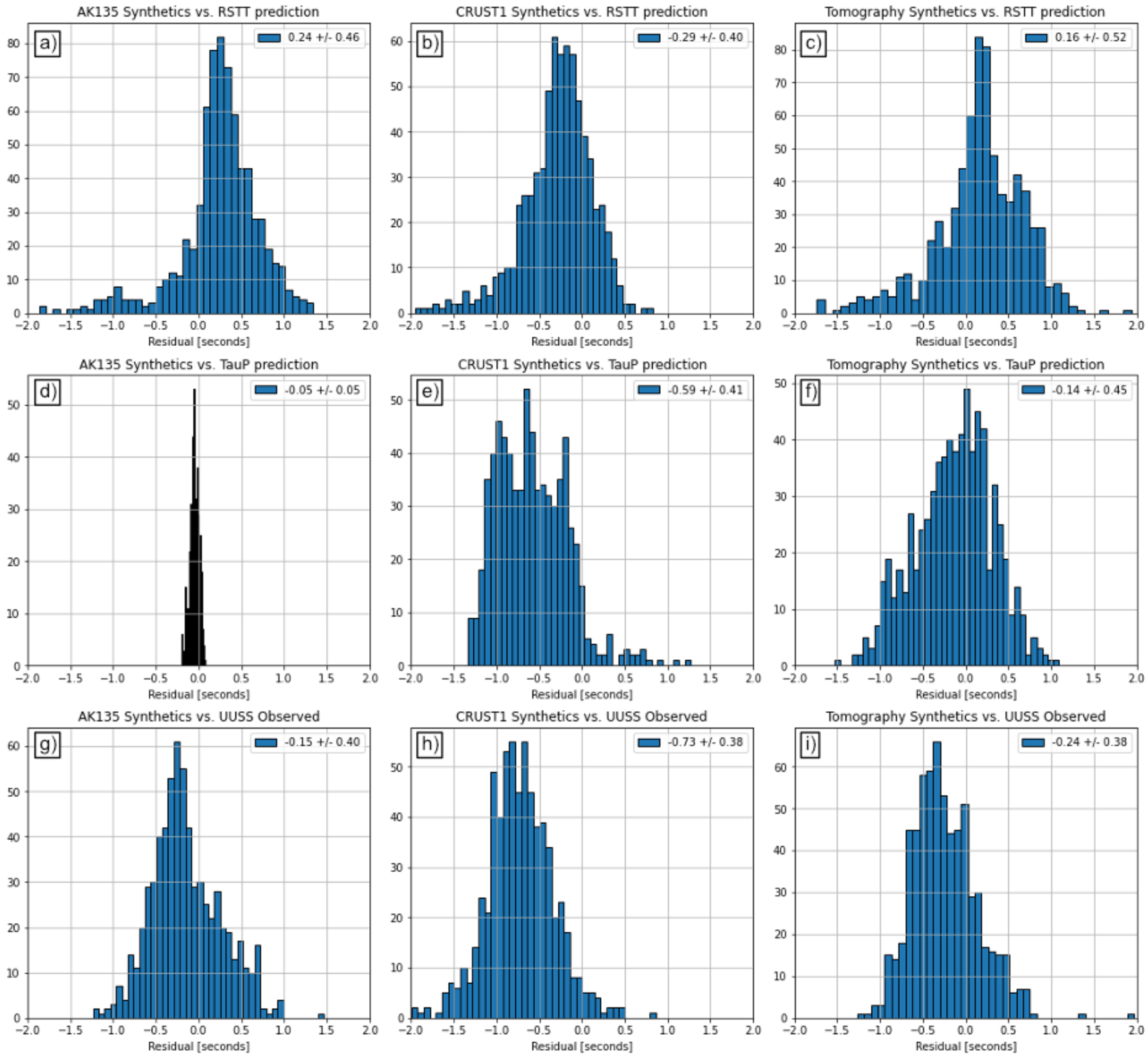

**Figure 2-4: Distributions of residuals between hand-picked arrival times on synthetic seismograms for a model based on AK135 (left column), CRUST1.0 (center column), and local earthquake tomography (right column) against predictions from RSTT (top row), TauP with AK135 (center row), and UUSS observations (bottom row). Mean and 1 standard deviation indicated for each distribution in the upper right.**

Considering the limits of variability in the tested models, we can expect misfits in crustal phase arrival times to be as large as 1 second (see Fig. 2-4e, mean plus 1 sigma standard deviation), but non-optimized times tend to be closer to about 0.3 seconds and optimized residuals can approach 0.1 seconds. This is comparable to analyst precision which can be expected to have uncertainties around 0.1 seconds in the worst-case scenarios (i.e., Fig. 2-4e). Rowe et al. (2009) previously found that while residual distributions all have standard deviations of ~1.6 seconds for mantle ray paths, zero-mean values can be achieved when replicating arrivals with a common wavespeed model and ray path. Our results agree with their findings, but we also observe that for the shorter paths of crustal phases, the standard deviation in residuals decreases by a factor of 4 (~0.4 seconds). We also find that complex crustal models, such as CRUST1.0 can result in significantly different arrival times than what is predicted from 1D models such as AK135 or the operational models used by the UUSS.

# 3. FREQUENCY CONTENT OF M2-5 EARTHQUAKES IN OKLAHOMA

As we are seeking to model smaller magnitude earthquakes and lower yield explosions, the high frequency signal is a more relevant part of the seismic spectrum than the lower frequency signals typically modeled with forward methods (e.g., Aki, 1967). This is due to the source-time function which reflects the time it takes for an earthquake to rupture or an explosion to detonate. Small events tend to have short source-time functions and the signal that propagates from these sources will be depleted in low frequencies and enriched in high frequencies. The high frequency signals can be exploited for various discrimination methods (e.g., Tibi et al., 2019), but validating these methods with synthetic seismograms remains computationally expensive.

We explore this magnitude dependence of the frequency content by comparing the amplitude spectrums of earthquakes in Oklahoma ranging from magnitude 2.9 to 5.6 recorded by USArray stations. This set of earthquakes is chosen because the M5.6 was successfully modeled by Chu and Helmberger (2014) with a relatively simple 1D model for an array of stations to the northeast of the source. Our earlier replication of this study found the data fits well at periods between 64 and 16 seconds, but at shorter periods the data fit quickly degrades. However, it was unclear whether this degradation of fit was due to shortcomings in the modeling method, problems with the 1D wavespeed model, or lack of signal at short periods for the moderate sized earthquake. In this section, we isolate this latter effect to explore the frequency content required to be modeled to fit relatively small events.

We utilize the Continuous Wavelet Transform (CWT) to compute amplitude spectra for both body wave and surface wave components of the seismograms for four earthquakes, M2.9, M3.7, M4.8, and M5.6 with origins in Oklahoma and recorded by the USArray (Fig. 3-1). The CWT is defined for an arbitrary time series s(t) as:

$$S_{\omega}(a,\tau) = \frac{1}{|a|^{\frac{1}{2}}} \int_{-\infty}^{\infty} s(t)\bar{\psi}\left(\frac{t-\tau}{a}\right) dt \tag{1}$$

where $\bar{\psi}$ is the complex conjugate of the wavelet function, $\tau$ is the wavelet time, and $a$ is the scale, which for the Morlet wavelet, is inversely proportional to frequency, and $\omega$ is the control parameter for the wavelet (Mallat, 1999). The amplitude spectrum is then defined as:

$$P_{ss}(a) = \sum_{\tau} S_{\omega}(a,\tau) * \overline{S_{\omega}}(a,\tau) \tag{2}$$

where $\tau$ is the analysis time window and $\overline{S_{\omega}}(a,\tau)$ is the complex conjugate of the CWT. Following Langston and Mousavi (2019), we use the CWT and time-scale gating to isolate early arriving, high frequency body waves, and late arriving, low frequency surface waves.

The seismic waveform data analyzed here consists of broadband recordings primarily from the USArray. Station locations, event locations, and origin times are shown in Figure 3-1. Waveforms with durations of 10 minutes were collected from each station to ensure both the body waves and surface waves were well captured. Horizontal channels were rotated into radial and transverse components and our analysis focuses on the transverse component to isolate the $S_n$ and Love wave arrivals. Preprocessing included removing a linear trend and applying a 5% Hann taper. For the record sections in Figure 3-2, the waveforms were further high-pass filtered before we applied the soft thresholding denoising algorithm of Langston and Mousavi (2019). For the amplitude spectrums in figures 3-3 to 3-5, high-pass filtering was not applied to avoid biasing the results.

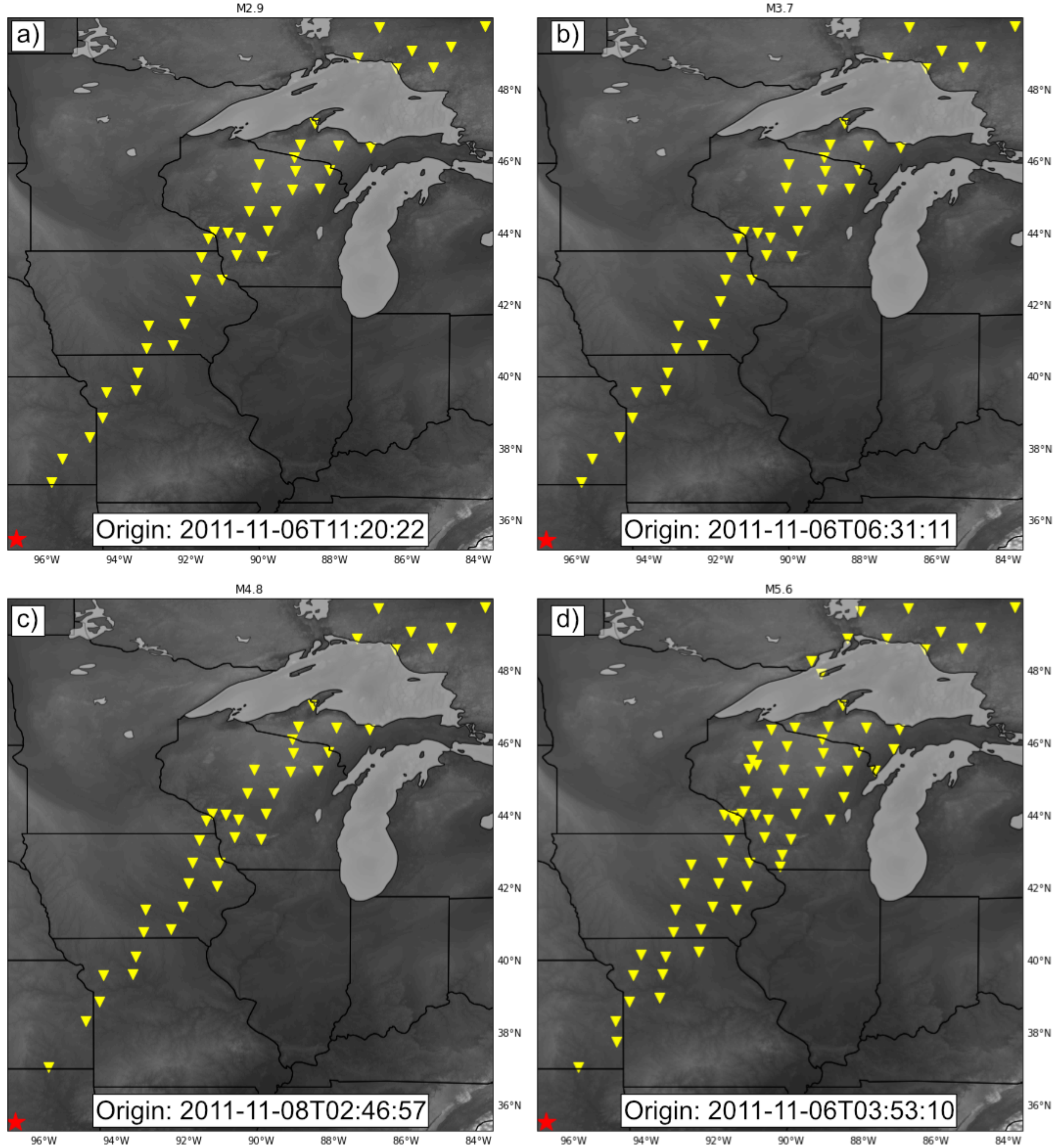

**Figure 3-1: Location maps of the 4 events analyzed here. Yellow triangles indicate broadband seismic stations and red stars indicate the source location. Origin time is given at the bottom of each panel. Panels: (a) M2.9, (b) M3.7, (c) M4.8, and (d) M5.6.**

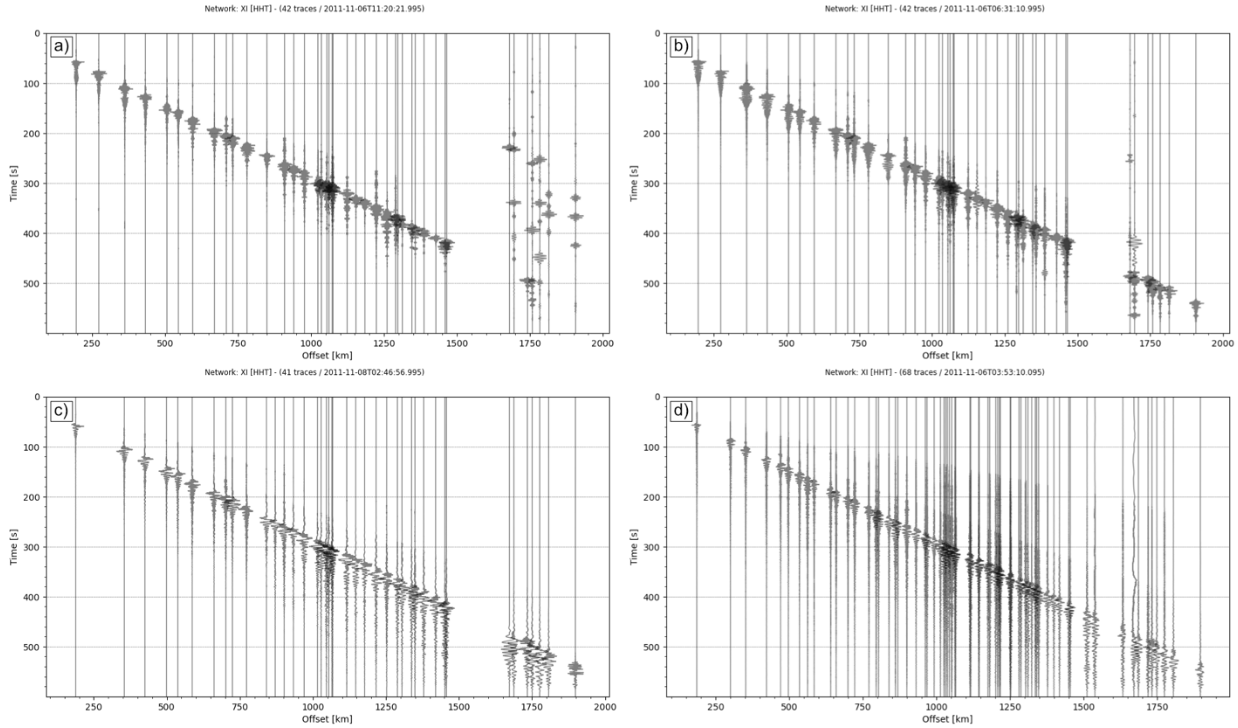

**Figure 3-2: Transverse component record sections for the 4 events in Oklahoma. Data has been filtered with hand-tuned passbands to highlight the signal and then denoised with soft thresholding (Langston and Mousavi, 2019). Panels: (a) M2.9, (b) M3.7, (c) M4.8, and (d) M5.6.**

Figures 3-3 to 3-5 present amplitude spectra as a function of frequency (i.e., reciprocal of Morlet wavelet scale) and distance between the source and receiver. Figure 3-3 shows the spectra summed over the entire 10-minute time series after optimal high-pass filtering and soft thresholding denoising whereas figures 3-4 and 3-5 show the spectra without the high-pass filter, but with soft threshold denoising and time-scale gating about the $S_n$ and Love waves respectively. In all cases, the expected trend of lower frequency signals for larger events can be observed. We also note that there is qualitative similarity between the M2.9 and M3.7 earthquake spectra and between the M4.8 and M5.6 earthquake spectra. Considering the full waveform (Fig. 3-3), much of the signal for the M2.9 and M3.7 earthquakes is found between 5 seconds period and 3 Hz whereas the M4.8 and M5.6 have little signal at frequencies above 5 seconds period. Focusing on the $S_n$ and its coda (Fig. 3-4), however, shows much greater variability. The M2.9 and M3.7 earthquake spectra have much of their signal above 1 Hz with an apparently increasing frequency with distance. The M4.8 shows the opposite trend with signal primarily below 1 Hz and generally decreasing frequency with distance. Interestingly, the M5.6 shows a bi-modal distribution with both high and low frequency trends with distance. This reflects both the complex energetics of the earthquake and a potential source of error from manually selecting a subspace. These body wave trends contrast sharply with the Love wave spectra (Fig. 3-5). These show little variation in maximum frequency as a function of distance but do show the trend of generally decreasing frequency with increasing magnitude.

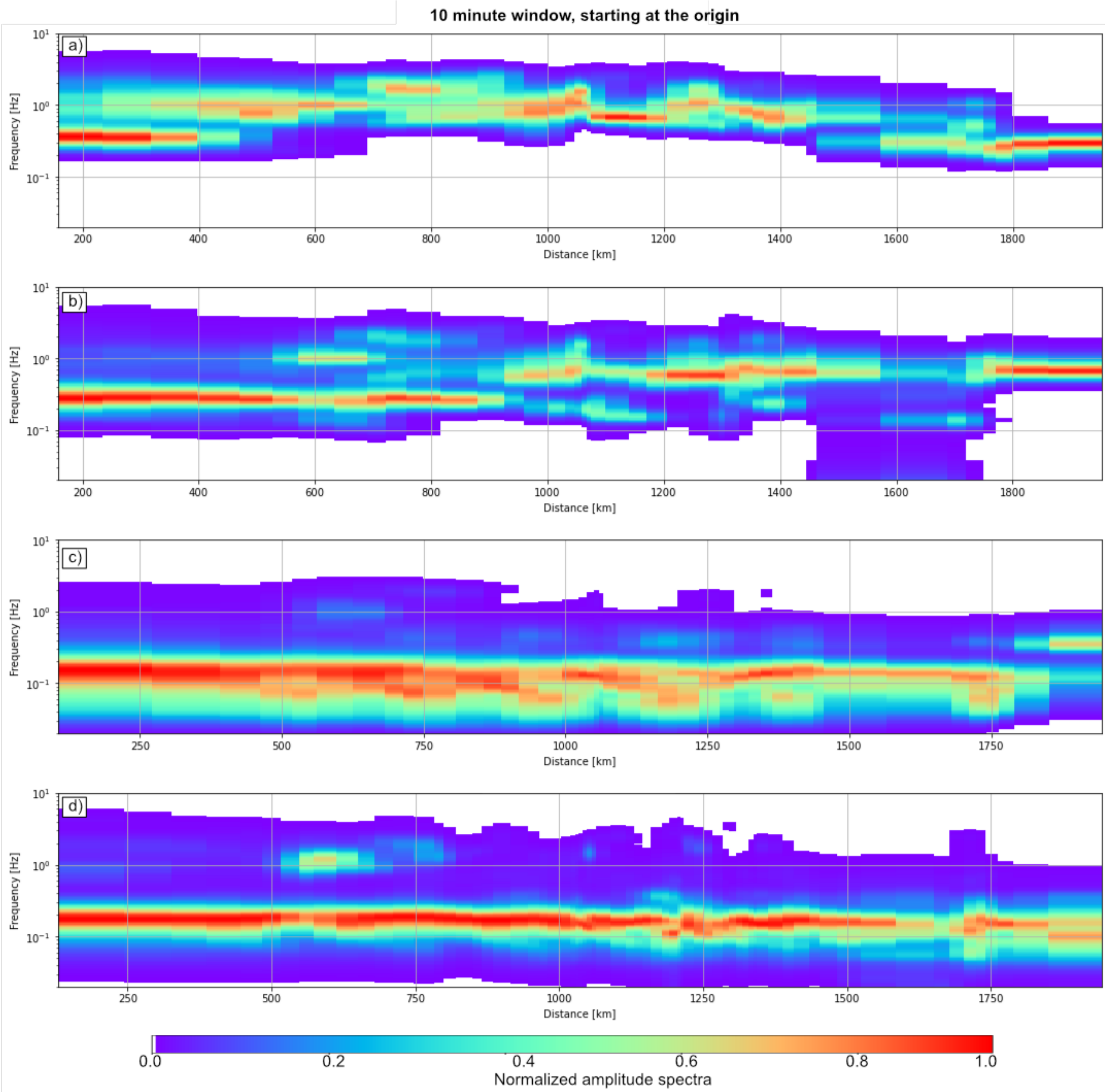

**Figure 3-3: Normalized wavelet amplitude spectra for the entire waveforms starting at the origin time with a duration of 10 minutes. Panels: (a) M2.9, (b) M3.7, (c) M4.8, and (d) M5.6.**

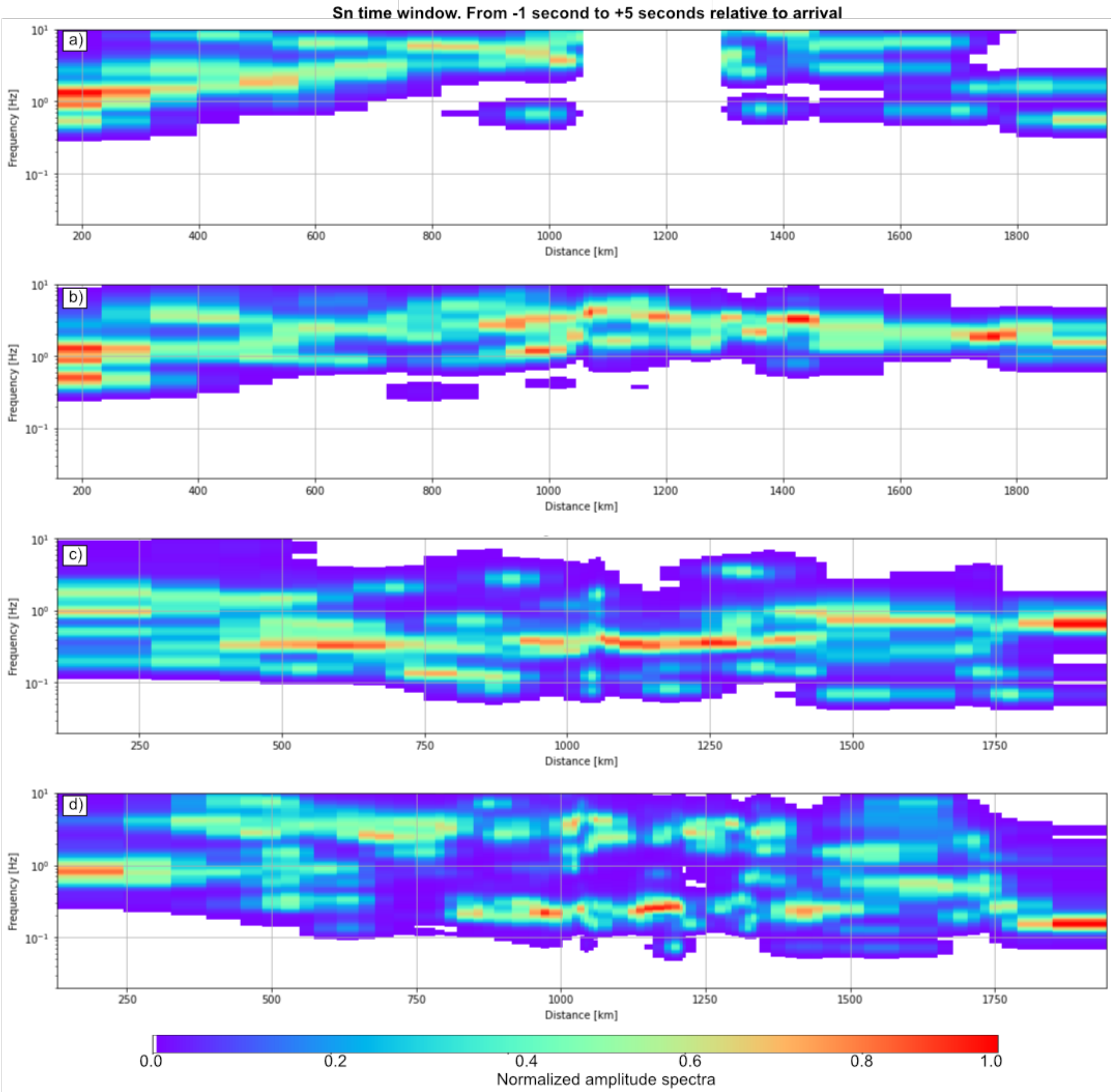

**Figure 3-4: Normalized wavelet amplitude spectra for $S_n$ arrival following wavelet time-scale gating about the observed arrival. Panels: (a) M2.9, (b) M3.7, (c) M4.8, and (d) M5.6.**

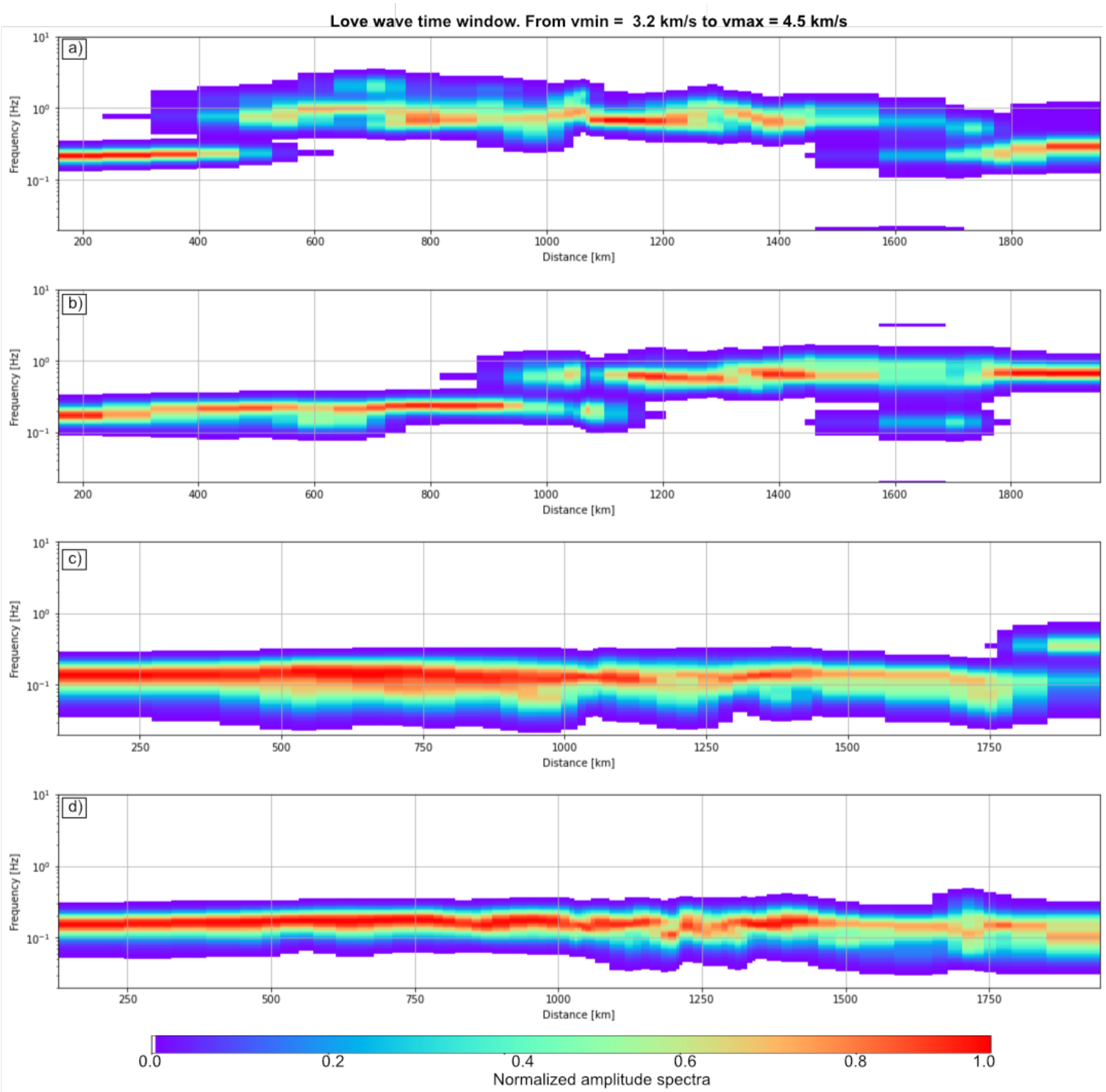

**Figure 3-5: Normalized wavelet amplitude spectra for Love wave following wavelet time-scale gating about the observed signal. Panels: (a) M2.9, (b) M3.7, (c) M4.8, and (d) M5.6.**

This analysis shows the commonly understood concept of larger earthquakes generating lower frequency signals and vice-versa, but with more detail and with the variable of unknown propagation structure removed. A surprising observation, however, is that the M4.8 tends to have slightly lower frequency content than the M5.6. This likely reflects two competing effects: (1) processing to isolate signals is a non-unique process and may introduce minor artifacts and (2) the resonant frequency of the sub-surface structure might be such that signals near 10 seconds are amplified. Furthermore, comparing the frequency content of the body waves and surface waves shows that small event surface waves contain relatively high frequency content that is difficult to separate from the body waves if there is little offset in arrival times. This presents a significant challenge to waveform modeling as the propagation paths, and therefore sensitivities, of body waves and surface waves are different, but not unrelated.

# 4. EFFECTS OF STOCHASTIC SCATTERING

As the seismic energy radiates from a source, the characteristics of the signal are modulated by the propagation medium. Our primary tool, travel-time tomography, is designed to constrain only a smoothed model of seismic wavespeeds within the medium and therefore is unable to fully capture how the wavefield is perturbed by the subsurface. This restriction exists for both body waves and surface waves and for local to teleseismic scales and is dependent on the frequency content of the observed signal and the coarseness of the wavespeed model. Nonetheless, because travel-times are the most straightforward property analysts can measure, are useful in locating events, and have linearized relationships to source and structure problems that have been derived, travel-time tomography remains the primary area of active research. However, a significant proportion of the observed seismic signal is coda. This signal is generated by near-surface scattering and has been shown to have relatively low attenuation at high frequencies (e.g., Aki and Chouet, 1975). This means that quantitatively fitting waveforms at high frequencies is dependent upon modeling attenuation in the shallow layers. A recent forward modeling study by Olsen et al. (2018) further illustrated this as they found significant improvements in the amplitude fit between their synthetics and a reported underground nuclear test after tuning the frequency dependent attenuation in their structural model. Moreover, this study found that tuning stochastic structural perturbations as a function of depth led to better simultaneous fits of $P_g$, $P_n$, and coda phases.

Rather than attempt to fit specific seismic amplitudes and phases or longer period representations such as envelopes, here we focus on isolating the effects on the waveforms after adjusting stochastic structural perturbations. This provides three key advantages over waveform fitting. First, it improves our understanding of the physical processes responsible for generating waveform phenomena. Second, it allows quantitative exploration of a much larger search space than relying on observed seismograms alone. Third, it provides a foundation to develop a new method of tomography that seeks to constrain parameters related to stochasticity rather than deterministic wavespeed. This section focuses on a single parameter, the amplitude of the perturbations, as it is relatively easy to assess the effect of perturbing this single variable. However, a full exploration of depth dependence and aspect ratio of scattering is ongoing.

We parameterize scattering as a Gaussian distribution of wavespeed anomaly shapes which are then scaled by the test parameter called the scale factor. A set of example cross-sections is shown in Figure 4-1. The background structure is the tomographic model of Preston and Hoots used in section 2 above with the addition of CRUST1.0 for the upper ~3 km and lower ~10 km. Synthetic waveforms are calculated with the 2D finite differences algorithm also used in section 2 with a Gaussian shaped source-time function with a duration of 0.2 seconds.

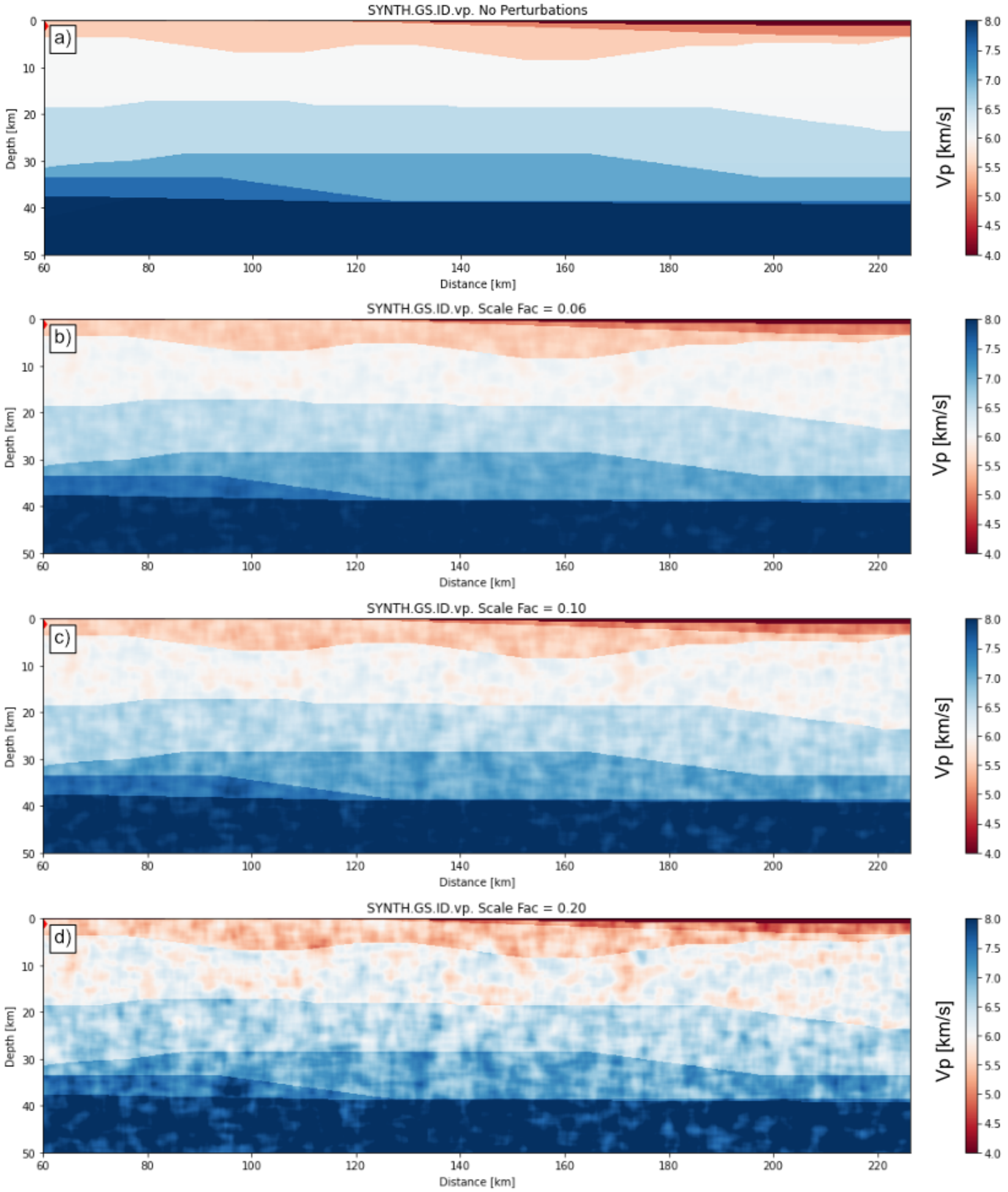

**Figure 4-1: Cross-sections of P wave wavespeed with increasing amplitude of stochastic perturbations. Scale Fac indicates the scale factor used to scale amplitudes while shapes are generated with a constant random seed.**

The waveforms from this test are presented in figures 4-2 and 4-3. Waveforms in Figure 4-2 are offset to facilitate tracking of changes as scale factor increases whereas Figure 4-3 presents them overlain to highlight bulk differences. Color-coding is the same in both figures. Differences between traces are generally subtle with the minimal difference at the direct P wave and most significant differences in the Rayleigh waves. In Fig. 4-2a, the most notable difference in the P wave is the decrease in relative phases between the direct arrival at ~8.5 seconds and the coda before ~12 seconds. For scale factors less than ~0.14, there are two phases with distinct amplitudes above the rest of the coda (labeled $P_1$ and $P_2$), but for larger scale factors, the amplitude of the P and P coda wave package is homogeneous. The double-couple source in Fig. 4-2b has a larger S wave relative to the P wave and the two arrival pulses, $S_1$ and $S_2$, are generally observable for most scale factors, but seem decreased in relative amplitude for scale factors of 0.08 to 0.10. At larger scale factors, 0.16 to 0.20, the two arrivals are less distinctive and rather there is an initial S arrival followed by a high amplitude packet.

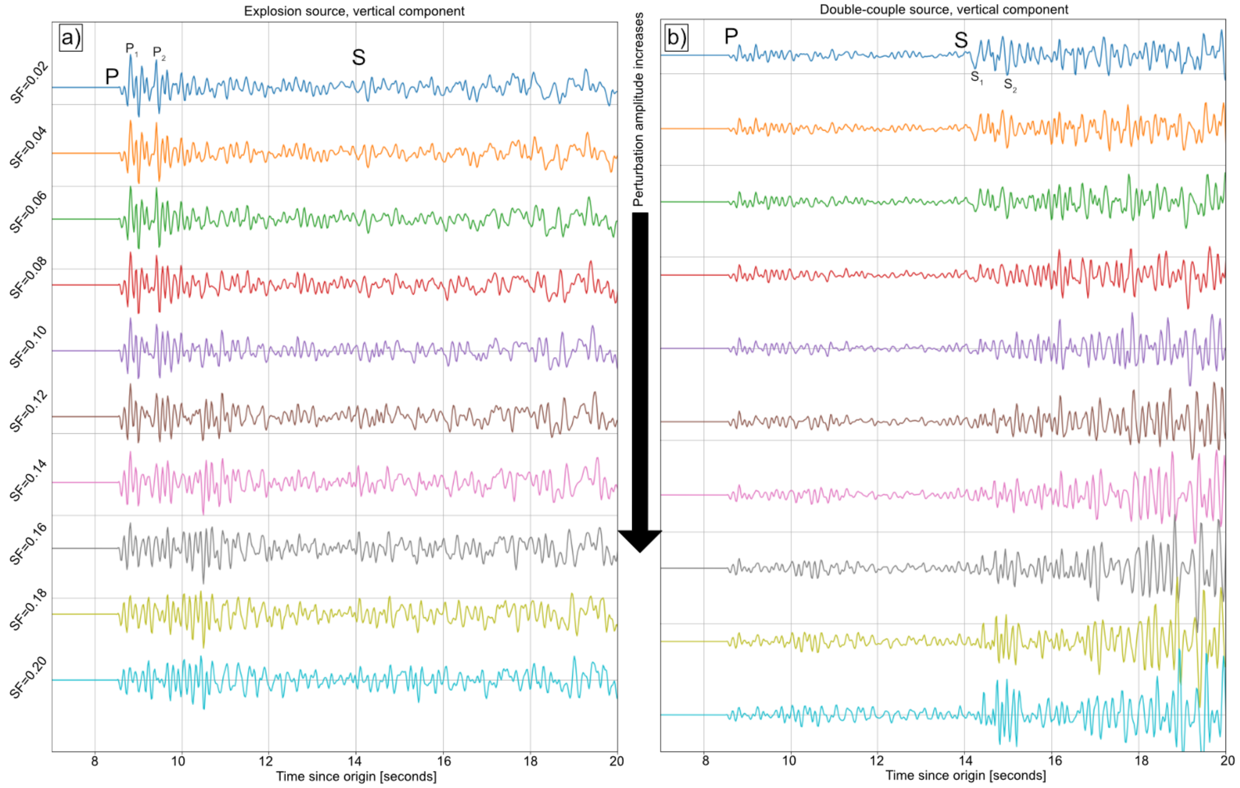

**Figure 4-2: Effect on vertical component waveforms as perturbation amplitude increases as per Fig. 4-1. Scale factor is labeled on the left as SF. Panels (a) and (b) are for explosion source and double couple source, respectively. P and S arrivals are labeled. All waveforms are for the same source-receiver path. Horizontal distance between source and receiver is 45 km and the source depth is 1 km. Time window is from 7 seconds after the origin to 20 seconds after the origin.**

Considering Figure 4-3, the initial P wave arrivals overlay nearly exactly for the first ~0.75 seconds. Following those first few cycles of the P wave signal, the P wave coda begins to be phase-shifted amongst the traces. Following the P coda, the S wave signals are also phase-shifted, but the differences become more apparent for surface waves arriving after ~16-18 seconds (group velocity of ~2.5 – 2.8 km/s). This increase in phase misalignment for the coda, S phases, and surface waves is expected as these phases have longer ray-paths through the heterogeneous structure being tested. The large offset in the double-couple late-arriving surface wave (Fig. 4-3d) is due to the significant travel time in the low wavespeed upper crust as those short period surface waves are primarily sensitive to the shallow wavespeed structure and their long travel-times accumulate more perturbations than the earlier arriving body waves.

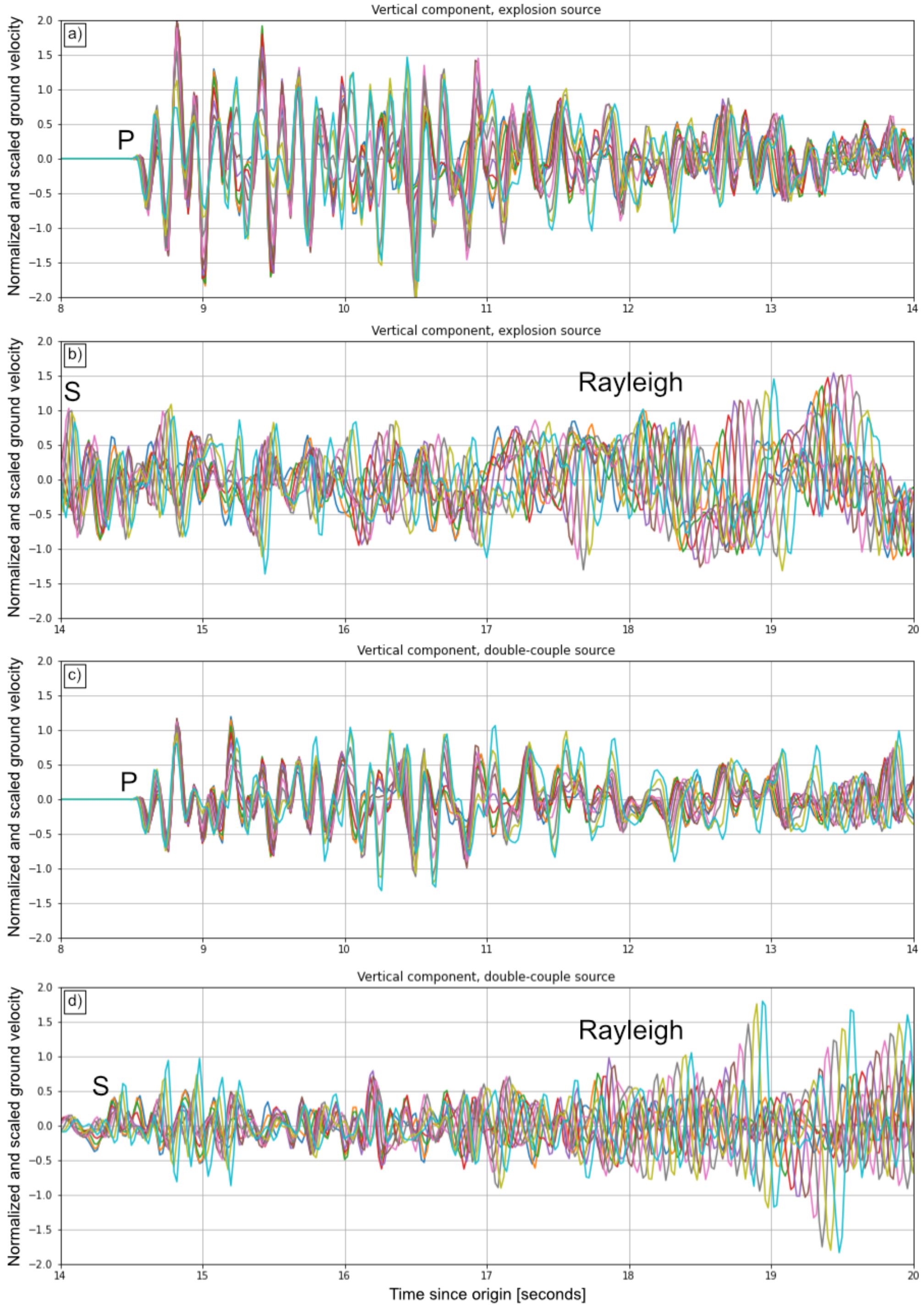

**Figure 4-3: Close up of overlain traces with varying scale factor from Fig. 4-2, cut to highlight specific phases. Different colored waveforms indicate different scale factors. Rayleigh surface wave is late arriving with group velocities between 2.3 and 2.8 km/s. Panel (a) is for an explosion source focused on the P arrival and coda. Panel (b) is the S arrival, S coda, and Rayleigh wave for an explosion source. Panel (c) is a double-couple source P wave and P coda (scaled up 4x relative to other panels). Panel (d) is S arrival, S coda, and Rayleigh wave for a double-couple source.**

There are various methods to quantify the variation in the observed synthetic seismograms. Here we apply a simple method of comparing the peak-to-peak amplitudes of the waveforms as we adjust the scale factor. These waveforms are not scaled to represent a specific earthquake magnitude or explosion yield and therefore this is only a relative comparison. In Figure 4-4, we see in both the explosion case and the double-couple case, the inclusion of stochastic perturbations (i.e., scale factor > 0) increases the peak-to-peak amplitude over the base case. However, the two cases have reversed concavity with the explosion case being concave up and the double-couple case being concave down. As this is a relatively small part of the possible search space, this relationship may not hold in general and thus will require further exploration to be confident in the result. Nonetheless, this shows that the amplitude of stochastic structural perturbations has a significant effect on both the phase and amplitude of seismic signals. Further research will be required to quantify how this effect interacts with the shapes of anomalous structures, long-wavelength wavespeed structure, and attenuation.

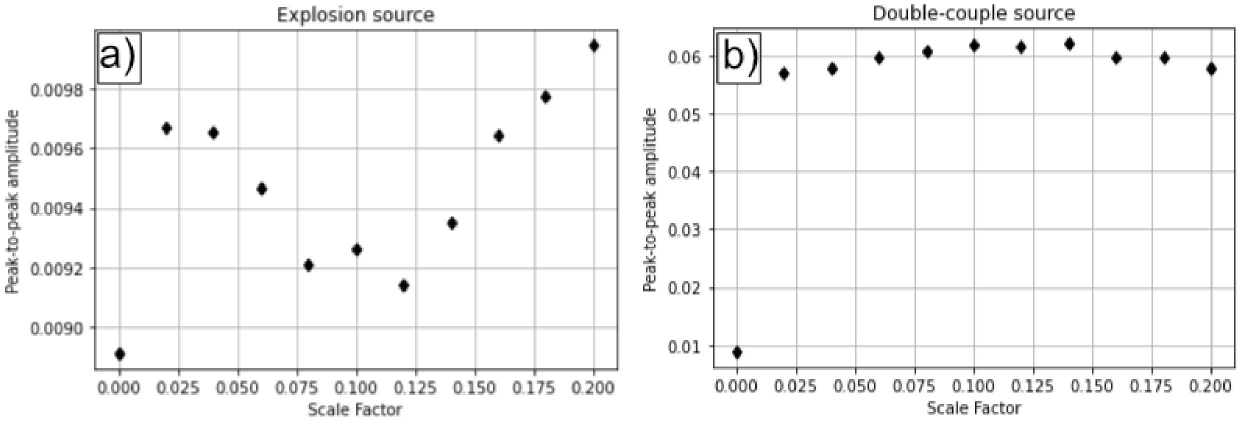

**Figure 4-4: Variation in the peak-to-peak amplitudes of the waveforms in figures 4-2 and 4-3 for (a) the explosion source and (b) for the double-couple source.**

## 5. CONCLUSIONS

In this report we have compared observed and calculated arrival times for both real earthquakes and synthetic earthquakes, compared the frequency content of magnitude 2.9 to 5.6 earthquakes as a function of distance, and explored the effect of stochastic scattering in a limited case. The key findings are:

- From the analysis of travel times, we expect residuals for crustal scale velocity models may approach 0.1 seconds between the observed and modeled arrival times of first arriving P phases and that residuals greater than ~0.5 seconds may indicate a problem.
- Based on our analysis of frequency content for various magnitude earthquakes, we find that earthquakes below ~M4 are depleted in low frequency energy and therefore require waveform modeling at frequencies above ~1 Hz.
- Finally, we find that adjusting the amplitude of stochastic scattering results in different effects between explosion sources and double-couple sources. These differences are apparent in both the phase shift of arrivals following the direct arrival and the peak-to-peak amplitudes of the waveforms.

In the next stage of this work we will seek to improve our models of structure at the crustal scale by a combination of travel time tomography and through developing stochasticity tomography. Ideally, this will allow us to accurately model both travel times and amplitudes for a global distribution of sources and receivers.

# REFERENCES

[1] Aki, K. (1967). Scaling law of seismic spectrum, *Journal of Geophysical Research*, **72** (4), pp. 1217-1231, doi:10.1029/JZ072i004p01217

[2] Aki, K. and Chouet, B. (1975). Origin of coda waves: Source, attenuation, and scattering effects, *Journal of Geophysical Research*, **80** (23), pp. 3322-3342, doi:10.1029/JB080i023p03322

[3] Ballard, S., Hipp, J. R., Young, C. J. (2009). Efficient and Accurate Calculation of Ray Theory Seismic Travel Time through Variable Resolution 3D Earth Models, *Seismological Research Letters*, **80** (6), pp. 989-999, doi:10.1785/gssrl.80.6.989

[4] Begnaud, M. L., Myers, S. C., Young, B., Hipp, J. R., Dodge, D. and Phillips, W. S. (2020). Updates to the Regional Seismic Travel Time (RSTT) Model: 1. Tomography, *Pure and Applied Geophysics*, **178**, pp. 2475-2498, doi:10.1007/s00024-020-02619-5

[5] Buland, R. and Chapman, C. H. (1983). The computation of seismic travel times, *Bulletin of the Seismological Society of America*, **73**, pp. 1271-1302, doi:10.1785/BSSA0730051271

[6] Chu, R. and Helmberger, D. V. (2014). Lithospheric waveguide beneath the Midwestern United States; massive low-velocity zone in the lower crust, *Geochemistry, Geophysics, Geosystems* **15**, 1348-1362, doi:10.1002/2013GC004914.

[7] Crotwell, H. P., Owens, T. J., and Ritsema, J. (1999). The TauP toolkit: flexible seismic travel-time and ray-path utilities, *Seismological Research Letters*, **70** (2), pp. 154-160, doi:10.1785/gssrl.70.2.154

[8] Fichtner, A., Kennett, B. L. N., Igel, H., and Bunge, H-P. (2010). Full waveform tomography for radially anisotropic structure: New insights into present and past states of the Australasian upper mantle, *Earth and Planetary Science Letters*, **290** (3-4), pp. 270-280, doi: 10.106/j.epsl.2009.12.003

[9] Hicks, E., Hoeber, H., Houbiers, M. Lescofit, S. P., Ratcliffe, A., and Vinje, V. (2016). Time-lapse full-waveform inversion as a reservoir-monitoring tool – A North Sea case study, *The Leading Edge*, **35** (10), doi:10.1190/tle35100850.1

[10] Kennett, B. L. N., Engdahl, E. R., and Buland, R. (1995). Constrains on seismic velocities in the Earth from travel times, *Geophysical Journal International,* **122**, pp. 108-124, doi:10.1111/j.1365-246X.1995.tb03540.x

[11] Lanza, F., Thurber, C. H., Syracuse, E. M., Power, J. A., and Ghosh, A. (2020). Seismic tomography of compressional wave velocity and attenuation structure for Makushin Volcano, Alaska, *Journal of Volcanology and Geothermal Research,* **393**, 106804, doi:10.1016/j.jvolgeores.2020.106804

[12] Laske, G., Masters, G., and Reif, C. (2001). CRUST 2.0: A New Global Crustal Model at 2x2 Degrees, https://igppweb.ucsd.edu/~gabi/crust2.html, accessed 09/03/2021

[13] Laske, G., Masters, G., Ma, Z., and Pasyanos, M. (2013). Update on CRUST1.0 – A 1-degree global model of Earth's crust, *European Geophysical Union* (Vol. 15, pp. EGU 2013-2658). https://igppweb.ucsd.edu/~gabi/crust1.html, accessed 09/03/2021

[14] Lekić, V. and Romanowicz, B. (2011). Inferring upper-mantle structure by full waveform tomography with the spectal element method, *Geophysical Journal International*, **185** (2), pp. 799-831, doi:10.1111/j.1365-246X.2011.04969.x

[15] Li, D., Helmberger, D. V., Clayton, R. W., and Sun, D. (2014). Global synthetic seismograms using a 2-D finite-difference method, *Geophysical Journal International,* **197**, 2, 1166-1183, doi:10.1093/gji/ggu050.

[16] Mallat, S. (1999). A wavelet tour of signal processing. Elsevier.

[17] Myers, S. C., Begnaud, M. L., Ballard, S., Pasyanos, M. E., Phillips, W. S., Ramirez, A. L., Antolik, M. S., Hutchenson, K. D., Dwyer, J. J., Rowe, C. A., and Wagner, G. S. (2010). A Crust and Upper-Mantle Model of Eurasia and North Africa for $P_n$ Travel-Time Calculation, *Bulletin of the Seismological Society of America*, **100** (2), pp. 650-656, doi:10.17850120090198

[18] Olsen, K. B., Begnaud, M., Phillips, S., Jacobsen, B. H. (2018). Constraints of Crustal Heterogeneity and Q(f) from Regional (< 4 Hz) Wave Propagation for the 2009 North Korea Nuclear Test, *Bulletin of the Seismological Society of America,* **108** (3A), pp. 1369-1383, doi:10.1785/0120170195

[19] Rowe, C. A., Ballard, S., Begnaud, M. L., Young, C. J., Steck, L. K., and Hipp, J. R. (2009). Validating 3D Geophysical Models for Use in Global Travel-Time Calculation for Improved Event Locations, *2009 Monitoring Research Review: Ground-Based Nuclear Explosion Monitoring Technologies*. NNSA. Accessed at https://www.ldeo.columbia.edu/res/pi/Monitoring/Doc/Srr_2009/PAPERS/02-15.PDF

[20] Takemura, S., Yabe, S., and Emoto, K. (2020). Modelling high-frequency seismograms at ocean bottom seismometers: effects of heterogeneous structures on source parameter estimation for small offshore earthquakes and shallow low-frequency tremors, *Geophysical Journal International,* **223**, pp. 1708-1723, doi:10.1093/gji/ggaa404

[21] Tape, C., Liu, Q., Maggi, A., and Tromp, J. (2010). Seismic tomography of the southern California crust based on spectral-element and adjoint methods, *Geophysical Journal International*, **180** (1), pp. 433-462, doi:10.1111/j.1365-246X.2009.04429.x

[22] Thurber, C. H. (1992). Hypocenter-velocity structure coupling in local earthquake tomography, *Physics of the Earth and Planetary Interiors,* **75** (1-3), pp. 55-62, doi:10.1016/0031-9201(92)90117-E

[23] Vidale, J. Helmberger, D. V., and Clayton, R. W. (1985). Finite-difference seismograms for SH waves, *Bulletin of the Seismological Society of America,* **175,** no. 6, 1765-1782.

[24] Zhang, H. and Thurber, C. H. (2003). Double-difference tomography: the method and its application to the Hayward fault, California, *Bulletin of the Seismological Society of America,* **93**, pp. 1875-1889, doi:10.1785/0120020190

This page left blank

# DISTRIBUTION

**Email—Internal**

| Name | Org. | Sandia Email Address |
|---|---|---|
| Andrea Conley | 06752 | acconle@sandia.gov |
| John Merchant | 06756 | bjmerch@sandia.gov |
| Technical Library | 01977 | sanddocs@sandia.gov |

**Email—External** [redacted]

| Name | Company Email Address | Company Name |
|---|---|---|
| Michael Begnaud | mbegnaud@lanl.gov | Los Alamos National Labs |
| Jeffrey Miller | jmiller@aftac.gov | AFTAC |
| Stephen Myers | myers30@llnl.gov | Lawrence Livermore National Labs |
| Jorge Roman-Nieves | jorge.roman-nieves.1@us.af.mil | AFTAC |
| Gregory Wagner | gwagner@aftac.gov | AFTAC |

This page left blank

This page left blank

Sandia National Laboratories